FISFVIER

Contents lists available at ScienceDirect

Applied Mathematical Modelling

journal homepage: www.elsevier.com/locate/apm





A Timoshenko-Ehrenfest beam model for simulating Langevin transducer dynamics

Yuchen Liu^a, Lu Trong Khiem Nguyen^{b,1}, Xuan Li^a, Andrew Feeney^{a,*}

- a Centre for Medical and Industrial Ultrasonics. University of Glasgow, James Watt School of Engineering, Glasgow, G12 800. United Kingdom
- ^b Glasgow Computational Engineering Centre, University of Glasgow, James Watt School of Engineering, Glasgow, G12 8LT, United Kingdom

ARTICLE INFO

Keywords: Langevin transducer Spectral element method Timoshenko beam Piezoelectricity

ABSTRACT

The Langevin transducer is a widely used power ultrasonic device across both medical and industrial applications, from orthopaedic surgery to drilling and welding. It is a sandwichtype device which typically consists of piezoelectric ceramic rings between two metallic endmasses. The transducer is commonly operated at a particular resonant mode to deliver ultrasonic vibrations to a target structure of interest, and is generally modelled using approaches including the transfer matrix method and electromechanical equivalent circuit methods. Here, we propose a variational framework to study the dynamics of the Langevin transducer based on the Timoshenko-Ehrenfest beam theory and Hamilton's principle. The variational equation derived from this model is then discretized by the standard finite element method with spectral elements. To verify the proposed one-dimensional electromechanical model, the computed resonance frequencies, or natural frequencies, of the one-dimensional model are compared to those of a three-dimensional finite element model with respect to varying geometry parameters characterizing the transducer. The results of the reduced one-dimensional and full threedimensional models are then compared to those measured through an experimental investigation consisting of laser Doppler vibrometry. This is undertaken for the first ten eigenfrequencies, including longitudinal and bending modes, where normalized amplitudes and vibration mode shapes are reported. The close correlation between modelling and experiment demonstrates that the proposed one-dimensional electromechanical model can deliver results consistent with the full three-dimensional model and from experiment, thus verifying a rapid and reliable method for studying the free vibrations and dynamics of the Langevin transducer which accounts for the axial vibrations of the piezoelectric ceramic stack in all cases.

1. Introduction

Langevin transducers are commonly used in both medical and industrial applications as the fundamental component of a power ultrasonic system, such as ultrasonic scalpels [1–3], drilling [4–6] and welding [7–9]. The fundamental configuration of Langevin transducers generally consists of a front mass, a back mass, a composite stack consisting of lead zirconate titanate (PZT) rings

E-mail address: Andrew.Feeney@glasgow.ac.uk (A. Feeney).

URL: https://www.gla.ac.uk/schools/engineering/staff/andrewfeeney/ (A. Feeney).

https://doi.org/10.1016/j.apm.2024.04.019

Received 13 July 2023; Received in revised form 23 February 2024; Accepted 8 April 2024

Available online 12 April 2024

0307-904X/© 2024 The Author(s). Published by Elsevier Inc. This is an open access article under the CC BY license (http://creativecommons.org/licenses/by/4.0/).

^{*} Corresponding author.

 $^{^{1}\,\,}$ The author contributed equally to this work.

with electrodes, and a preloading bolt which is used to compress the entire configuration together [10,11]. This straightforward configuration makes manufacturing convenient, and there is generally reliable output power achievable given the relatively high degree of control possible on the transducer manufacturing process.

When an electrical input is applied to the PZT stack, the transducer can vibrate freely to achieve specific vibration mode shapes, such as longitudinal, bending, and torsional modes [12,13], and it is common for the Langevin transducer to be tailored to low ultrasonic frequencies, with modal behaviours tuned in the 20 kHz to 100 kHz range [14]. The Langevin transducer has been the subject of detailed study for many years, both experimentally [15–18] and through linear piezoelectricity based simulation [19,20]. It is crucial to simulate dynamic properties such as resonance frequency and mode shape, especially through the electromechanical coupling model since dynamic properties are highly dependent on electrical input [21,22]. The electromechanical model of the Langevin transducer can be constructed in terms of the constitutive relations of piezoelectric materials [23–25]. As a guide to the design process, simulation results should be precise thus ensuring consistency with experimental results and reducing the demands on time involved in design.

Mathematical methods have been devised to study the dynamics of ultrasonic transducers. For example, the transfer matrix method [26–28], analytical modelling [29–31], and equivalent circuit method [32–34] are three of the most frequently used approaches. In these methods, the key idea is to establish the dynamic relationship between the resultant forces and the generalized degrees of freedom at the boundaries of each component of the transducer. However, up to this point, no electromechanical model has been proposed to account for the axial motions of the PZT stack in each vibration mode, including those such as bending motions of the transducer which will still generate such axial motions. When a voltage is applied to the PZT stack to drive the transducer, it experiences an axial strain caused by the electrical field parallel to the polarization direction [35], irrespective of the vibration mode shape utilised. Thus, the axial strain of the excited PZT stack, and consequently the axial displacement, should be properly accounted for in the analytical beam model.

To incorporate the axial motions of the piezoelectric ceramic stack and to develop a numerically effective tool for simulating the dynamics of the Langevin transducer, a one-dimensional (1D) Timoshenko-Ehrenfest beam model is proposed, as a reduction of the full three-dimensional (3D) model. It is important to note that this beam consists of several segments made of three different materials, two of which can be modelled as isotropic elastic materials, and the other as a transversely isotropic piezoelectric material. These segment structures are generalised as a solid beam with a circular cross-section, a solid beam with an annular cross-section, and a composite beam with the combination of circular and annular cross-sections.

Regarding the constitutive modelling of piezoelectric materials, the strain-charge relationship is utilised to describe the strain responses in the presence of the electric field [36]. The variational principle is developed for the 1D model by the reduction of the 3D constitutive law to the 1D version. This is a significant and novel development, as there has not yet been any variational framework established for a composite beam made of multiple elastic and piezoelectric materials, and is a primary contribution to knowledge from this research. The equations of motion for the entire transducer are then derived, based on Hamilton's principle [37,38]. The corresponding variational principle is subsequently discretized and solved by using the spectral element method.

To demonstrate that 1D model is robust and can be applied with high accuracy, the results of the 1D model and that of the full 3D model obtained by the finite element analysis (FEA) software ABAQUS/CAE (Dassault Systémes) are compared across a range of Langevin transducer configurations with respect to different length-to-diameter (L/D) ratios and PZT stack length ratios. However, since there are no standard guidelines for designing Langevin transducers, a set of correlation conditions have been established in this research, in which each structural parameter is varied as a linear function of the approximation of the corresponding practical value. Further validation is conducted by comparing results from the 3D model against that of a manufactured Langevin transducer whose dynamic properties are measured using a 3D scanning laser Doppler vibrometer (LDV). The benefits of using 3D LDV are that it analyses vibration on complex surfaces and ensures the scanned grid points are sufficient in terms of resolution for comparison with the 1D model [39]. The excellent agreement between the results extracted from the 1D and 3D models, and the experimental results using the LDV, demonstrate the validity and reliability of the proposed mathematical and computational framework.

This article consists of the following key novel contributions. First, a new variational framework for modelling the entire Langevin transducer is demonstrated, including accounting for axial vibration behaviour of the piezoelectric stack, based on the Timoshenko-Ehrenfest beam theory [40,41]. Subsequently, the governing equations and the corresponding boundary conditions are then derived, and this is detailed in Section 2. Secondly, the discretization of the variational equation using the finite element method and spectral elements is reported in Section 3, before the results of the reduced 1D and full 3D models are compared by varying the L/D, PZT stack length ratios, and electric potentials, detailed in Section 4. It is anticipated that this modelling strategy will be used to develop improved electromechanical models for a wide range of ultrasonic transducer configurations, and to tailor devices for particular industrial and medical applications.

2. Development of the Timoshenko-Ehrenfest beam model

2.1. Configuration of the Langevin transducer

The Langevin transducer utilised for this study is a cylindrical configuration without a horn-type amplifier, as shown in Fig. 1, showing the transducer's front mass, a back mass, a PZT stack with electrodes, and a preloading bolt. The electrodes are orders of magnitude thinner than the PZT rings and the front and back masses, and contribute an insignificant effect on the transducer dynamics. Therefore, they are not considered in this study, to reduce the calculation complexity and computation time. In response

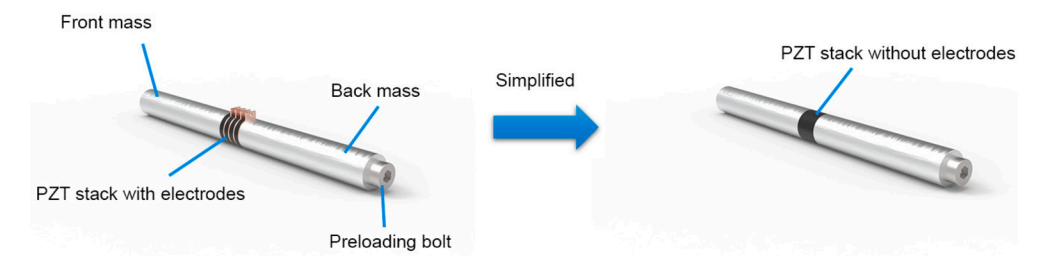


Fig. 1. The cylindrical Langevin transducer of the form used in this study.

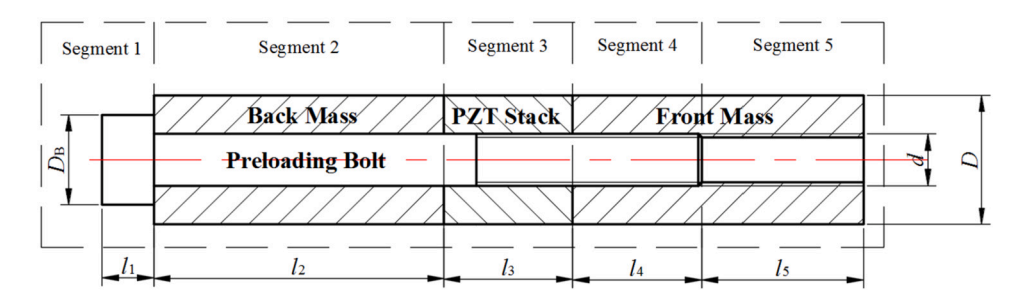


Fig. 2. Configuration of the Langevin transducer with respect to different segments.

to this assumption, the PZT stack will be considered as a homogeneous hollow cylinder made of piezoelectric materials in the modelling (see Fig. 1).

Each part of the Langevin transducer can be simplified into a straight beam due to its axial symmetry. It will be demonstrated later in this article that the transducer can be split into five different beam segments, each of which can be effectively modelled by a composite beam made of two orthotropic piezoelectric materials with poling directions along the symmetric axis, or the beam axis.

2.2. Problem definition

The transducer with the configuration as shown in Fig. 1 can be modelled using five different beam segments with different geometries and different materials, yielding a practically representative case. In this section, the geometries and materials of these segments are described in detail.

Geometry. First, from Fig. 2 the dimensions of each component in one beam segment can be readily identified. For example, the j^{th} segment, denoted as S_j , has the length I_j for all $j=\overline{1,5}$. The bolt contains the bolt head as a cylinder with the diameter D_B and the bolt screw as a cylinder with the diameter d. The back mass, the PZT stack, and the front mass are all hollow cylinders with annulus-type cross sections. They share the same outer diameter D and the same inner diameter D and connect to each other to make up one full hollow cylinder. Since this hollow cylinder is longer than the bolt screw, the entire transducer must be divided into five beam segments to enable accurate numerical modelling.

Material. The bolt, including the bolt head and bolt screw, is made of A2 tool steel. The back mass and the front mass are made of titanium Ti6Al4V. The PZT stack is made of PIC181, following the standard specification of the manufacturer (PI Ceramic GmbH). The magnitudes of the material constants for these materials will be given in detail in the subsequent section.

2.3. Material laws

To allow a comprehensive overview of the problem, an account of the basic theory of piezoelectric materials relevant to this research is provided here, which adheres to the IEEE Standard on Piezoelectricity [42]. In this theory, there are four distinguishable forms of constitutive relationships, comprising Stress-Charge; Stress-Voltage; Strain-Charge; and Strain-Voltage, with regards to input variables and their corresponding outputs, as detailed in Table 1. In this table, ϵ and σ denote the linear strain tensor and the Cauchy stress tensor, respectively, while the $\bf E$ and $\bf D$ denote the vector electric field and the induced electric displacement vector field, respectively. The linear strain tensor and the electric field are defined as gradients of the displacement vector field $\bf u$ and the electric potential field ϕ , respectively, according to:

$$\boldsymbol{\varepsilon} = \frac{1}{2}(\nabla \mathbf{u} + \mathbf{u}\nabla), \quad \mathbf{E} = -\nabla \phi. \tag{1}$$

For comparison with the experimental setup described in Section 4, the constitutive law in Stress-Charge form is employed, given as follows:

Table 1
Four forms of constitutive relationships relevant to this study

| Form | Constitutive relationship | | |
|----------------|---|--|--|
| Stress-Charge | $(\varepsilon, \mathbf{E}) \xrightarrow{\mathbb{C}_{\mathbf{E}=0}, \chi_{\varepsilon=0}} (\sigma, \mathbf{D})$ | | |
| Strain-Charge | $(\sigma,E) \xrightarrow{\S_{E=0},\chi_{\sigma=0}} (\varepsilon,D)$ | | |
| Stress-Voltage | $(\varepsilon, \mathbf{D}) \xrightarrow{\mathbb{C}_{\mathbf{D}=0}, \chi_{\varepsilon=0}^{-1}} (\sigma, \mathbf{E})$ | | |
| Strain-Voltage | $(\sigma,D) \xrightarrow{\S_{D=0},\chi_{\sigma=0}^{-1}} (\varepsilon,E)$ | | |

$$\sigma = \mathbb{C}_{E=0} : \varepsilon - e^T \cdot E,$$

$$D = e : \varepsilon + \gamma_{\varepsilon = 0} \cdot E.$$
(2)

The tensors of the constitutive coefficients in this constitutive relation are explained as follows. The fourth-order tensor $\mathbb{C}_{E=0}$ is the elastic stiffness obtained in the absence of an electric field (E=0). The second-order tensor $\chi_{\epsilon=0}$ is the electric permittivity tensor obtained in the absence of mechanical strain $(\epsilon=0)$. The third-order tensor \mathbf{e} is the piezoelectric coupling coefficient for the Stress-Charge form. The double dot and single dot denote the double contraction and the dot product between two tensors, respectively. It is convenient to suppress the subscripts in the tensors of material properties and thus the following can be written: $\mathbb{C}:=\mathbb{C}_{E=0}$, $\gamma:=\chi_{\epsilon=0}$.

On the other hand, the material properties for PIC181 provided from the manufacturer specifications correspond to the constitutive law in the Strain-Charge form:

$$\varepsilon = \mathbb{S}_{E=0} : \sigma + \mathbf{d}^T \cdot \mathbf{E},$$

$$\mathbf{D} = \mathbf{d} : \sigma + \gamma_{\sigma=0} \cdot \mathbf{E}.$$
(3)

In this constitutive formulation, $\mathbb{S}_{E=0}$ is the compliance stiffness in the absence of the electric field (E=0), $\gamma_{\sigma=0}$ is the electric permittivity in the absence of mechanical stress $(\sigma=0)$, and d denotes the piezoelectric coupling coefficients for the Strain-Charge form. Again, the shorthand $\mathbb{S} := \mathbb{S}_{E=0}$ and $\gamma := \gamma_{\sigma=0}$ can be used. Comparing (3) with (2), one can readily derive:

$$\mathbb{C} = \mathbb{S}^{-1}, \quad \mathbf{e} = \mathbf{d} : \mathbb{S}^{-1}, \quad \gamma = \gamma - \mathbf{d} \cdot \mathbb{S}^{-1} \cdot \mathbf{d}^{T}, \tag{4}$$

where \mathbb{S}^{-1} represents the inverse of the fourth-order tensor of \mathbb{S} .

Just as for hyperelastic materials, the constitutive law (2) can be derived as partial derivative of an enthalpy density function. It is given by:

$$\psi(\boldsymbol{\varepsilon}, \mathbf{E}) = \frac{1}{2}\boldsymbol{\varepsilon} : \mathbb{C} : \boldsymbol{\varepsilon} - \mathbf{E} \cdot \mathbf{e} : \boldsymbol{\varepsilon} - \frac{1}{2}\mathbf{E} \cdot \boldsymbol{\chi} \cdot \mathbf{E}. \tag{5}$$

The constitutive relation (2) can be obtained by identifying:

$$\sigma = \frac{\partial \psi}{\partial \varepsilon}, \quad \mathbf{D} = -\frac{\partial \psi}{\partial \mathbf{E}}.$$
 (6)

Here, by considering (2), the enthalpy density function can be rewritten as follows:

$$\psi = \frac{1}{2}(\epsilon : \sigma - \mathbf{E} \cdot \mathbf{D}). \tag{7}$$

The density function (5) can be used to describe deformations of isotropic materials. Indeed, in this case only the elastic strain energy density, namely the first term of (5), is considered, so that the stress is given by standard Hooke's law $\sigma = \mathbb{C}$: ϵ .

2.4. Variational framework

As the poling of the PZT material is in the direction of the beam axis, the axial displacement of the beam cross-section must also be considered. It is important to note that this is different from the classical Timoshenko beam theory, which normally only considers the bending [43,44]. Let us assume that the beam axis is in the *z*-direction and the beam cross-section is the *xy*-plane. The starting point here is the assumption of the displacement field $\mathbf{u} = (u_1, u_2, u_3)$ of the material in the beam as follows:

$$u_1(x, y, z, t) = 0,$$

 $u_2(x, y, z, t) = w(z, t),$
 $u_3(x, y, z, t) = u(z, t) - y\varphi(z, t),$
(8)

where u_1, u_2, u_3 are the components of the displacement vector **u** in the three coordinate directions, u is the axial displacement of the cross-section, φ is the angle of rotation of the normal to the cross-section surface, and w is the deflection of the neutral axis in the z-direction. According to this, the strain field is given by:

$$\boldsymbol{\varepsilon} = \frac{1}{2} (\nabla \mathbf{u} + \mathbf{u} \nabla) = \begin{bmatrix} 0 & 0 & 0 \\ 0 & 0 & \frac{1}{2} (w_{,z} - \varphi) \\ 0 & \frac{1}{2} (w_{,z} - \varphi) & u_{,z} - y \varphi_{,z} \end{bmatrix}. \tag{9}$$

Therefore, the non-zero components of the strain field ε are ε_{23} , ε_{32} , and ε_{33} .

2.4.1. Reduction of the 3D constitutive law to 1D

To derive the variational formulation for the beam model of transducer, the 1D reduction of the aforementioned 3D laws is required. By using the Voigt notation following the IEEE Standard [42], the tensors of material properties in (2) can be represented as matrices. In particular, the elastic tensor and the piezoelectric coupling tensor are given as matrices $\mathbf{C} \in \mathbb{R}^{6\times6}$, $\mathbf{e} \in \mathbb{R}^{3\times6}$ and $\chi \in \mathbb{R}^{3\times3}$.

In general, reduction of the 3D constitutive law (2) to the lower-dimensional law also depends on the electric field, because the non-zero components of \mathbf{E} can influence the form of the reduced law. In this work, the electric potential field is applied along the beam axis direction so that $E_3 \neq 0$ is the only non-zero component. Following this assumption, the non-zero stress and electric displacement components can be derived as follows:

$$\sigma_{33} = C_{33}\varepsilon_{33} - e_{33}E_{3}, \quad \sigma_{23} = 2\kappa C_{23}\varepsilon_{23}, \quad D_3 = e_{33}\varepsilon_{33} + \chi_{33}E_{3}, \tag{10}$$

where κ is the shear correction coefficient [45,46]. As for the computation, the shear correction coefficient for a circular cross-section is employed:

$$\kappa_{\text{circular}} = \frac{6(1+\nu)}{7+6\nu},\tag{11}$$

and this can also be applied for an annular cross-section:

$$\kappa_{\text{annulus}} = \frac{6(1+\nu)(1+\alpha^2)^2}{(7+6\nu)(1+\alpha^2)^2 + (20+12\nu)\alpha^2}, \quad \alpha = \frac{d_o}{d_i}$$
(12)

where d_i and d_o are the inner and outer diameters of the annulus, and ν is the Poisson's ratio. The material constants appearing in (10) are obtained using the relation (4) and the material properties provided by PI Ceramic GmbH. Then, only the relevant material constants are used. One important point to note here is that for isotropic elastic materials, only $\sigma_{33} = C_{33}\varepsilon_{33}$ and $\sigma_{23} = 2\kappa C_{23}\varepsilon_{23}$ are required.

Therefore, consistent with the 1D law (10), the enthalpy density function reduces to the 1D version:

$$\psi_{1D}(\epsilon, \mathbf{E}) = \frac{1}{2}(\sigma_{33}\epsilon_{33} + 2\sigma_{23}\epsilon_{23}) - \frac{1}{2}D_3E_3. \tag{13}$$

2.5. Derivation of the equations of motion

2.5.1. General consideration

In this section, the variational equation for a beam segment made of transversely isotropic piezoelectric materials is derived, from where the equations of motion for the Langevin transducer can then be derived. In particular, the beam geometry is described by a cylinder assumed to be ideally bonded with a right circular hollow cylinder, or a cylindrical shell. These two cylinders are made of two different piezoelectric materials with poling in the z-direction. Although no beam segment in the simulated transducer has the above-mentioned material and geometrical description, the derivation can still be applicable to all five beam segments for two reasons:

- 1. The constitutive model for an isotropic elastic material can be specified as the reduced model for a transversely isotropic piezoelectric material.
- 2. A composite beam with the cylinder perfectly bonded with a right circular hollow cylinder, or a cylindrical shell, is a generalization of the homogeneous cylinder beam.

The geometrical and material setup for five beam segments are shown in Fig. 3. For the above reasons, the variational equation for a homogeneous beam of isotropic elastic material or a composite beam of elastic and piezoelectric materials has been incorporated in the subsequent derivation.

2.5.2. Total stored and kinetic energies

First, the formulation for one beam segment can be detailed. Let the coordinates of the two ends of the beam segment be z = a on the left and z = b on the right (a < b). Then, the total stored energy of the beam is given by:

$$W = \int_{a}^{b} \int_{A} \frac{1}{2} (\sigma_{33} \epsilon_{33} + 2\sigma_{23} \epsilon_{23} - D_3 E_3) dA dz$$

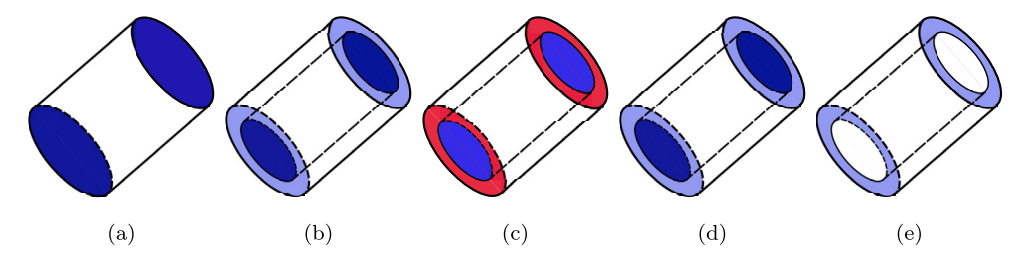


Fig. 3. Geometrical and material definitions for the five beam segments representing the entire Langevin transducer, where the colours on the cross-sections designate the following: (1) dark blue for steel; (2) light blue for titanium; and (3) red for PIC181, showing (a) Segment 1: Cylinder made of isotropic elastic material, (b) Segment 2: Cylinder wrapped by a hollow cylinder made of two different isotropic elastic materials, (c) Segment 3: Cylinder made of isotropic material wrapped by hollow cylinder made of transversely isotropic piezoelectric material, (d) Segment 4: Cylinder wrapped by a hollow cylinder made of two different isotropic elastic materials, and (e) Segment 5: Hollow cylinder composed of isotropic material.

$$= \int_{a}^{b} \int_{A} \frac{1}{2} (C_{33} \varepsilon_{33}^{2} - 2e_{33} E_{3} \varepsilon_{33} + 4\kappa C_{23} \varepsilon_{23}^{2} - \chi_{33} E_{3}^{2}) dA dz,$$
(14)

where A denotes the cross-sectional area of the beam segment. The total stored energy W is a functional of the functions u, w, φ and ϕ , or alternatively expressed as $W = W[u, w, \varphi, \phi]$, by recalling that:

$$\varepsilon_{23} = (w_z - \varphi)/2, \quad \varepsilon_{33} = u_z - y\varphi_z, \quad E_3 = -\varphi_z.$$
 (15)

Substituting (15) into (14), it can be shown that:

$$W = \int_{a}^{b} \int_{A} \left[\frac{1}{2} C_{33} (u_{,z}^{2} + y^{2} \varphi_{,z}^{2}) + e_{33} u_{,z} \phi_{,z} \right.$$

$$\left. + \frac{1}{2} \kappa C_{23} (w_{,z}^{2} - 2w_{,z} \varphi + \varphi^{2}) - \frac{1}{2} \chi_{33} \phi_{,z}^{2} \right] dAdz,$$

$$(16)$$

where the following identity has been taken into account:

$$\int_{A} y dA = 0. \tag{17}$$

Note that equation (17) is valid because the neutral axis is across the centre of the circular cross-section. If the cross-section is not a disk, the property (17) is not always true because a composite beam which is being studied is made of two out of three different materials (see, e.g., [47]). The kinetic energy for the beam segment is given by:

$$T = \int_{a}^{b} \int_{A} \rho \sum_{i=1}^{3} u_{i,t}^{2} dA dz = \int_{a}^{b} \int_{A} \rho \left[w_{,t}^{2} + (u_{,t} - y\varphi_{,t})^{2} \right] dA dz$$

$$= \int_{a}^{b} \int_{A} \rho (w_{,t}^{2} + u_{,t}^{2} + y^{2}\varphi_{,t}^{2}) dA dz$$
(18)

where ρ is the material density distribution in the beam segment and again (17) has been used.

Since a beam segment made of one cylinder and one hollow cylinder is considered, each of which is modelled by different materials, the integral over the cross-section must be split according to the following:

$$\int_{A} (\diamond) dA = \int_{A(1)} (\diamond) dA + \int_{A(2)} (\diamond) dA,$$
(19)

where $A^{(1)}$ stands for the circular cross-section and $A^{(2)}$ for the annulus cross-section. Let r_1 and r_2 denote the radius of the inner cross-section and the outer cross-section, respectively. Then, the areas of the circular and the annulus cross-sections are given by:

$$A^{(1)} = \pi r_1^2, \quad A^{(2)} = \pi (r_2^2 - r_1^2).$$
 (20)

Similarly, the moment of inertia for the two different cross-sections can be computed as:

$$I_1 = \int_{A^{(1)}} y^2 dA = \pi r_1^4, \quad I_2 = \int_{A^{(2)}} y^2 dA = \pi (r_2^4 - r_1^4). \tag{21}$$

In the following derivation, the superscripts $(\diamond)^{(1)}$ and $(\diamond)^{(2)}$ are used to designate the material constants for two piezoelectric materials, for example, $C_{33}^{(1)}$, $C_{33}^{(2)}$ and so on. With this denotation, (16) can be rewritten as:

$$W = \sum_{j=1}^{2} \int_{a}^{b} \left[\frac{1}{2} A^{(j)} C_{33}^{(j)} u_{,z}^{2} + \frac{1}{2} C_{33}^{(j)} I^{(j)} \varphi_{,z}^{2} + A^{(j)} e_{33}^{(j)} u_{,z} \phi_{,z} \right.$$

$$\left. + \frac{1}{2} A^{(j)} \kappa^{(j)} C_{23}^{(j)} (w_{,z} - \varphi)^{2} - \frac{1}{2} A^{(j)} \chi_{33}^{(j)} \phi_{,z}^{2} \right] dz$$

$$(22)$$

Similarly, the kinetic energy then becomes:

$$T = \sum_{j=1}^{2} \int_{a}^{b} \frac{1}{2} \left[A^{(j)} \rho^{(j)} (u_{,t}^{2} + w_{,t}^{2}) + I^{(j)} \rho^{(j)} \varphi_{,t}^{2} \right] dz.$$
 (23)

The geometrical constants and the material constants appearing in the above stored energy and kinetic energy can be combined, to shorten the formulation and thus benefit the subsequent derivation. In particular, the following 'composite' constants are introduced:

$$AC_{33} = \sum_{j=1}^{2} A^{(j)} C_{33}^{(j)}, \quad A\kappa C_{23} = \sum_{j=1}^{2} A^{(j)} \kappa^{(j)} C_{23}^{(j)},$$

$$Ae_{33} = \sum_{j=1}^{(2)} A^{(j)} e_{33}^{(j)}, \quad IC_{33} = \sum_{j=1}^{2} I^{(j)} C_{33}^{(j)}, \quad A\chi_{33} = \sum_{i=1}^{2} A^{(j)} \chi_{33}^{(j)},$$

$$A\rho = \sum_{j=1}^{2} A^{(j)} \rho^{(j)}, \quad I\rho = \sum_{j=1}^{(2)} I^{(j)} \rho^{(j)}.$$
(24)

It is important to note that the composite constants introduced above should not be confused with the multiplication of two constants as if the beam is made of homogeneous material.

To derive the stored energy and the kinetic energy for the entire transducer, the stored and kinetic energy functionals must be added for all five segments. To this end, the superscript $(\diamond)^{[s]}$ shall be used to denote the quantities for the beam segment s, including the composite constants defined above and the energy functional. For example, $W^{[s]}$ and $T^{[s]}$ denote the stored energy and the kinetic energy for the beam segment s, respectively, and $AC_{33}^{[s]}$ is the composite constant for the segment s. Also, it is assumed that the beam segment s spans from the coordinate $z=z_s$ to $z=z_{s+1}$. Therefore, the integral limits a and b in (26) for the beam segment s will be replaced by z_s and z_{s+1} , respectively. The total potential, defined as the difference between the kinetic energy and the stored energy, is given as:

$$\Pi = \sum_{s=1}^{N_s} (T^{[s]} - W^{[s]}),\tag{25}$$

with $N_s = 5$ being the number of the beam segments. In this expression, the stored energy $W^{[s]}$ and the kinetic energy $T^{[s]}$, $s = \overline{1, N_s}$, are given by:

$$W^{[s]} = \int_{z_{s}}^{z_{s+1}} \left[\frac{1}{2} A C_{33}^{[s]} u_{,z}^{2} + \frac{1}{2} I C_{33}^{[s]} \varphi_{,z}^{2} + A e_{33}^{[s]} u_{,z} \phi_{,z} \right.$$

$$\left. + \frac{1}{2} A \kappa C_{23}^{[s]} (w_{,z} - \varphi)^{2} - \frac{1}{2} A \chi_{33}^{[s]} \phi_{,z}^{2} \right] dz,$$

$$T^{[s]} = \int_{z_{s}}^{z_{s+1}} \frac{1}{2} \left[A \rho^{[s]} (u_{,t}^{2} + w_{,t}^{2}) + I \rho^{[s]} \varphi_{,t}^{2} \right] dz.$$

$$(26)$$

2.5.3. Establishing the variational equation

Taking the variation of $W^{[s]}$ with respect to u, w, φ and ϕ , the following equation can be obtained:

$$\delta W^{[s]} = \int_{z_{s}}^{z_{s+1}} \left[(AC_{33}^{[s]}u_{,z} + Ae_{33}^{[s]}\phi_{,z})\delta u_{,z} + A\kappa C_{23}^{[s]}(w_{,z} - \varphi)\delta w_{,z} \right. \\ \left. + IC_{33}^{[s]}\varphi_{,z}\delta\varphi_{,z} - A\kappa C_{23}^{[s]}(w_{,z} - \varphi)\delta\varphi \right. \\ \left. + (Ae_{33}^{[s]}u_{,z} - A\chi_{33}^{[s]}\phi_{,z})\delta\phi_{,z} \right] dz$$

$$(27)$$

where δu , δw , $\delta \varphi$ are the test functions corresponding to u, w, φ , ϕ , respectively. Note that the variation $\delta W^{[s]}$ expressed above is the Gateaux derivative of the functional $W^{[s]}$ at (u, w, φ, ϕ) in the direction $(\delta u, \delta w, \delta \varphi, \delta \phi)$.

The variation of the kinetic energy (18) is given by:

$$\delta T^{[s]} = \int_{z_{-}}^{z_{s+1}} \left[A \rho^{[s]} (u_{,t} \delta u_{,t} + w_{,t} \delta w_{,t}) + I \rho^{[s]} \varphi_{,t} \delta \varphi_{,t} \right] \mathrm{d}z \tag{28}$$

The motion of the transducer is governed by Hamilton's principle:

$$\delta \int_{t_0}^{t_1} \left[\sum_{s=1}^{N_s} (W^{[s]} - T^{[s]}) \right] = \int_{t_0}^{t_1} \sum_{s=1}^{N_s} (\delta W^{[s]} - \delta T^{[s]}) = 0, \tag{29}$$

where t_0 and t_1 are the initial time and the end time of the motion and considered as given. Substituting (27) and (28) into (29), it is possible to obtain the variational equation governing the motion of the transducer. Solving the variational equation by the finite element method will be the topic of the next section.

2.5.4. Governing equations and boundary conditions

Differential governing equations. Essentially, the variational equation described by (29) can be solved by the finite element method. However, for the purpose of completeness, the differential equations governing the motion of the transducer are also derived. By applying integration by parts to (27) with respect to the variable z, it can be shown that:

$$\begin{split} \int_{t_0}^{t_1} \delta W^{\{s\}} &= \int_{t_0}^{t_1} \left[(A C_{33}^{\{s\}} u_{,z} + A e_{33}^{\{s\}} \phi_{,z}) \delta u \right]_{z_s}^{z_{s+1}} \mathrm{d}t \\ &- \int_{t_0}^{t_1} \int_{z_s}^{z_{s+1}} (A C_{23}^{\{s\}} u_{,zz} + A e_{33}^{\{s\}} \phi_{,zz}) \delta u \, \mathrm{d}z \, \mathrm{d}t \\ &+ \int_{t_0}^{t_1} \left[A \kappa C_{23}^{\{s\}} (w_{,z} - \varphi) \delta w \right]_{z_s}^{z_{s+1}} \, \mathrm{d}t \\ &- \int_{t_0}^{t_1} \int_{z_s}^{z_{s+1}} A \kappa C_{23}^{\{s\}} (w_{,zz} - \varphi_{,z}) \delta w \, \mathrm{d}z \, \mathrm{d}t \\ &+ \int_{t_0}^{t_1} \left[I C_{33}^{\{s\}} \varphi_{,zz} \delta \varphi \right]_{z_s}^{z_{s+1}} \, \mathrm{d}t \\ &- \int_{t_0}^{t_1} \int_{z_s}^{z_{s+1}} \left[I C_{33}^{\{s\}} \varphi_{,zz} + A \kappa C_{23}^{\{s\}} (w_{,z} - \varphi) \right] \delta \varphi \, \mathrm{d}z \, \mathrm{d}t \\ &+ \int_{t_0}^{t_1} \left[(A e_{33}^{\{s\}} u_{,z} - A \chi_{33}^{\{s\}} \phi_{,z}) \delta \phi \right]_{z_s}^{z_{s+1}} \, \mathrm{d}t \\ &+ \int_{t_0}^{t_1} \left[(A \chi_{33}^{\{s\}} \phi_{,zz} - A e_{33}^{\{s\}} u_{,zz}) \delta \phi \, \mathrm{d}z \, \mathrm{d}t, \end{split}$$

where the denotation $[f(z)]_{z_s}^{z_{s+1}} = f(z_{s+1}) - f(z_s)$ has been used. As for the contribution of kinetic energy from Hamilton's principle (29), integration by parts can be employed with respect to t to obtain:

$$\int_{t_0}^{t_1} \delta T^{[s]} dt = \int_{t_0}^{t_1} \int_{z_{s-1}}^{z_{s+1}} \left[-A \rho^{[s]} (u_{,tt} \delta u + w_{,tt} \delta w) - I \rho^{[s]} \varphi_{,tt} \delta \varphi \right] dz dt, \tag{31}$$

where the condition that δu , δw and $\delta \varphi$ vanish at both $t = t_0$ and $t = t_1$ has been applied.

Substituting (30) and (31) into (29), it can be demonstrated that:

$$\sum_{s=1}^{N_{1}} \left\{ \int_{t_{0}}^{t_{1}} \left[(AC_{33}^{[s]}u_{,z} - Ae_{33}^{[s]}\phi_{,z})\delta u \right]_{z_{s}}^{z_{s+1}} dt \right.$$

$$\left. + \int_{t_{0}}^{t_{1}} \int_{z_{s}}^{z_{s+1}} \left[A\rho^{[s]}u_{,tt} - AC_{33}^{[s]}u_{,zz} - Ae_{33}^{[s]}\phi_{,zz} \right] \delta u \, dz dt$$

$$\left. + \int_{t_{0}}^{t_{1}} \left[A\kappa C_{23}^{[s]}(w_{,z} - \varphi)\delta w \right]_{z_{s}}^{z_{s+1}} \, dt$$

$$\left. + \int_{t_{0}}^{t_{1}} \int_{z_{s}}^{z_{s+1}} \left[A\rho^{[s]}w_{,tt} - A\kappa C_{23}^{[s]}(w_{,zz} - \varphi_{,z}) \right] \delta w \, dz dt$$

$$\left. + \int_{t_{0}}^{t_{1}} \int_{z_{s}}^{z_{s+1}} \left[IC_{33}^{[s]}\varphi_{,z}\delta \varphi \right]_{z_{s}}^{z_{s+1}} \, dt$$

$$\left. + \int_{t_{0}}^{t_{1}} \int_{z_{s}}^{z_{s+1}} \left[I\rho^{[s]}\varphi_{,tt} - IC_{33}^{[s]}\varphi_{,zz} - A\kappa C_{23}^{[s]}(w_{,z} - \varphi) \right] \delta \varphi \, dz dt$$

$$\left. + \int_{t_{0}}^{t_{1}} \int_{z_{s}}^{z_{s+1}} \left[Ae_{33}^{[s]}u_{,z} - A\chi_{33}^{[s]}\varphi_{,zz} \right) \delta \varphi \, dz dt \right\} = 0$$

$$\left. + \int_{t_{0}}^{t_{1}} \int_{z_{s}}^{z_{s+1}} \left[Ae_{33}^{[s]}u_{,zz} - A\chi_{33}^{[s]}\varphi_{,zz} \right] \delta \varphi \, dz dt \right\} = 0$$

As δu , δw , $\delta \varphi$ and $\delta \varphi$ can vary arbitrarily on each interval (z_s, z_{s+1}) , $s = 1, \dots, N_s$, the following system of equations can be obtained:

$$A\rho^{[s]}u_{,tt} - AC_{33}^{[s]}u_{,zz} - Ae_{33}^{[s]}\phi_{,zz} = 0,$$

$$A\rho^{[s]}w_{,tt} - A\kappa C_{23}^{[s]}(w_{,zz} - \varphi_{,z}) = 0$$

$$I\rho^{[s]}\varphi_{,tt} - IC_{33}^{[s]}\varphi_{,zz} - A\kappa C_{23}^{[s]}(w_{,z} - \varphi) = 0,$$

$$Ae_{33}^{[s]}u_{,zz} - A\chi_{33}^{[s]}\phi_{,zz} = 0$$

$$(33)$$

for all $z \in (z_s, z_{s+1})$ and $s = \overline{1, N_s}$. This system must be accompanied by the boundary conditions derived from the boundary terms appearing in (32).

Reduction of differential equations. Through deriving this system, it has been argued that the variables δu , δw , $\delta \varphi$ and $\delta \varphi$ can vary arbitrarily in the sub-domain (z_s, z_{s+1}) . However, it is important to note that the validity of this argument depends on the considered beam segments. The explanation for this is as follows.

- 1. As for the beam segments [1], [2], [4], [5], these beam segments are not made of piezoelectric material but only isotropic elastic materials, and so the electric field potential ϕ can be neglected in the modelling. Thus, for these beam segments, only the mechanical displacement fields, namely u, w, φ , are the unknown fields in the system. Moreover, as these beam segments are modelled using the isotropic materials, $Ae_{33}^{[s]} = 0$ and $A\chi_{33}^{[s]} = 0$ for s = 1, 2, 4, 5 can be readily set. The longitudinal displacement u in these beam segments persists and depends on the applied electric field on the boundaries of the beam segment [3] because the displacement u in this beam segment [3] will transfer to the others via the resultant forces.
- 2. As for the beam segment [3], the electric field potential ϕ is required for the modelling and thus the unknown variables involve not only the mechanical displacement fields mentioned above but also ϕ .

Boundary conditions. The derivation of the boundary conditions for the transducer consisting of different beam segments is slightly more sophisticated than the derivation for one homogeneous beam. Indeed, the reason is that the resultant forces at the interfaces between the connecting beam segments must be in equilibrium. The boundary conditions at the two ends of the total beam, namely z = 0 and $z = z_{N_s+1} = L$ can be easily identified by setting the appropriate boundary terms in (32) to zero. However, at the interfaces between two connecting beam segments s and s+1, the boundary conditions are identified by equating the boundary terms evaluated

at the right end of beam segment s to the boundary terms evaluated at the left-end of the section s + 1. To this end, the following set of boundary conditions can be derived:

$$\begin{split} \left[(AC_{33}^{[1]}u_{,z} - Ae_{33}^{[1]}\phi_{,z})\delta u \right]_{z=0} &= 0, & \left[(AC_{33}^{[N_s]}u_{,z} - Ae_{33}^{[N_s]}\phi_{,z})\delta u \right]_{z=L} &= 0, \\ \left[A\kappa C_{23}^{[1]}(w_{,z} - \varphi)\delta w \right]_{z=0} &= 0, & \left[A\kappa C_{23}^{[N_s]}(w_{,z} - \varphi)\delta w \right]_{z=L} &= 0, \\ \left[IC_{33}^{[1]}\varphi_{,z}\delta\varphi \right]_{z=0} &= 0, & \left[IC_{33}^{[N_s]}\varphi_{,z}\delta\varphi \right]_{z=L} &= 0, \\ \left[(Ae_{33}^{[1]}u_{,z} - A\chi_{33}^{[1]}\phi_{,z})\delta\phi \right]_{z=0} &= 0, & \left[(Ae_{33}^{[N_s]}u_{,z} - A\chi_{33}^{[N_s]}\phi_{,z})\delta\phi \right]_{z=L} &= 0, \end{split}$$

$$(34)$$

and

$$\left[(AC_{33}^{[s]}u_{,z} - Ae_{33}^{[s]}\phi_{,z}) \right]_{z=z_{s}^{+}} + \left[(AC_{33}^{[s]}u_{,z} - Ae_{33}^{[s]}\phi_{,z}) \right]_{z=z_{s+1}^{-}} = 0,
\left[A\kappa C_{23}^{[s]}(w_{,z} - \varphi) \right]_{z=z_{s}^{+}} + \left[A\kappa C_{23}^{[s]}(w_{,z} - \varphi) \right]_{z=z_{s+1}^{-}} = 0,
\left[IC_{33}^{[s]}\varphi_{,z} \right]_{z=z_{s}^{+}} + \left[IC_{33}^{[s]}\varphi_{,z} \right]_{z=z_{s+1}^{-}} = 0,
\left[(Ae_{33}^{[s]}u_{,z} - A\chi_{33}^{[s]}\phi_{,z}) \right]_{z=z_{s}^{+}} + \left[(Ae_{33}^{[s]}u_{,z} - A\chi_{33}^{[s]}\phi_{,z}) \right]_{z=z_{s+1}^{-}} = 0,$$
(35)

for $s=2,\ldots,N_s-1$, where the notation $[f(z)]_{z=a^\pm}=\lim_{z\to a^\pm}f(z)$ means the limit of f(z) from the left and from the right of a, respectively.

3. Finite element analysis for the Langevin transducer

In this section, we discuss not only the discretization of the variational equation (29) by the finite element method but also the numerical procedure for computing the natural frequencies of the Langevin transducer. The first step is to establish the finite element model for (29), with $\delta W^{[s]}$ and $\delta T^{[s]}$ given by (27) and (31). The standard conforming finite element method is adopted, only focusing on constructing the stiffness and mass matrices at the element level (see [48]). Further to this, the spectral element method is used for the discretization [49]. For further background in spectral methods, readers are referred to [50].

3.1. Finite element setup

Let us assume the problem domain $\Omega=(0,L)$ for the transducer beam is discretized into N_e non-overlapping finite elements $\Omega^{(e)}$, i.e., $\Omega=\bigcup_{e=1}^{N_e}\Omega^{(e)},\ \Omega^{(m)}\cap\Omega^{(n)}=\emptyset$ for $m\neq n$. As for the shape functions on the finite elements, Lagrange polynomials of order p-1 are used. Let $H_j=H_j(\xi)$ for $j=\overline{1,p}$ denote the shape functions on the reference domain $\mathcal{R}=[-1,1]$ supported by the Chebyshev points $\xi_j=-\cos\left(j\frac{\pi}{n}\right)$ (see Fig. 4). The isoparametric mapping from the reference domain \mathcal{R} to the element $\Omega^{(e)}$ is defined by:

$$z^{(e)}(\xi) = \sum_{i=1}^{p} z_{i}^{(e)} H_{j}(\xi), \tag{36}$$

where $z_j^{(e)}$ are the coordinates of the nodes in the element $\Omega^{(e)}$. If the $\{z_j^{(e)}\}_{j=1}^p$ are defined following the same distribution pattern of $\{\xi_j\}_{j=1}^p$, then the reference-to-physical mapping (36) becomes a linear mapping. The mapping (36) changes from element to element and its inverse mapping from $\Omega^{(e)}$ to $\mathcal R$ will be denoted $\xi^{(e)} = \xi^{(e)}(z)$. The shape functions defined on the physical coordinate z are then given by:

$$N_j^{(e)}(z) = H_j(\xi^{(e)}(z)).$$
 (37)

Next, the trial functions u, w, φ, ϕ and their corresponding test functions $\delta u, \delta w, \delta \varphi, \delta \phi$ defined on the element $\Omega^{(e)}$ are interpolated according to:

$$f^{(e)}(z) = \sum_{i=1}^{p} N_j^{(e)}(z) f_j^{(e)}, \tag{38}$$

where f stands for the trial functions as well as test functions and $f_j^{(e)}$ are the corresponding degrees of freedom associated with the element $\Omega^{(e)}$. In this work, we use the shape functions of the same polynomial order p for all the finite elements. Let us denote

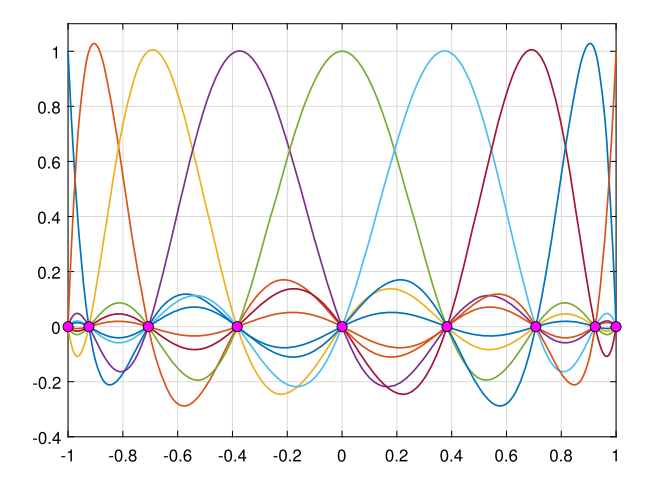


Fig. 4. Chebyshev points and Lagrange polynomials supported by these points as shape functions. The Chebyshev supporting nodes are defined by $\xi_j = \cos(j\pi/p)$ with n being the number of nodes for one element (circles filled by magenta). In this figure, p = 9 and thus the shape functions are polynomials of order p - 1 = 8.

by boldface notation $\mathbf{f}^{(e)}$ the column vector of degrees of freedom $f_j^{(e)}$ in the element $\Omega^{(e)}$, i.e., $\mathbf{f}^{(e)} = \begin{bmatrix} f_1^{(e)} & \cdots & f_p^{(e)} \end{bmatrix}^T$. This notation applies across the trial function functions u, w, φ, ϕ and the test functions $\delta u, \delta w, \delta \varphi, \delta \phi$, e.g., $\mathbf{u}^{(e)} = \begin{bmatrix} u_1^{(e)} & \cdots & u_p^{(e)} \end{bmatrix}^T$.

3.2. Element stiffness and mass matrices

To derive the stiffness matrices at the element level, the variation in (27) is used, that is the variational equation before application of the integration by parts. Indeed, by substituting the interpolations of type (38) into (27), the following can be obtained:

$$\delta W^{[s],(e)} = \delta \mathbf{u}^{(e)} \cdot \left[\mathbf{K}_{\mathbf{u}\mathbf{u}}^{(e)} \mathbf{u}^{(e)} + \mathbf{K}_{\mathbf{u}\boldsymbol{\phi}}^{(e)} \boldsymbol{\phi}^{(e)} \right] + \delta \mathbf{w}^{(e)} \cdot \left[\mathbf{K}_{\mathbf{w}\mathbf{w}}^{(e)} \mathbf{w}^{(e)} + \mathbf{K}_{\mathbf{w}\boldsymbol{\phi}}^{(e)} \boldsymbol{\varphi}^{(e)} \right] \\
+ \delta \boldsymbol{\varphi}^{(e)} \cdot \left[\mathbf{K}_{\boldsymbol{\varphi}\boldsymbol{\varphi}}^{(e)} \boldsymbol{\varphi}^{(e)} + \mathbf{K}_{\boldsymbol{\varphi}\mathbf{w}}^{(e)} \mathbf{w}^{(e)} \right] + \delta \boldsymbol{\phi}^{(e)} \cdot \left[\mathbf{K}_{\boldsymbol{\phi}\mathbf{u}}^{(e)} \mathbf{u}^{(e)} + \mathbf{K}_{\boldsymbol{\phi}\boldsymbol{\phi}}^{(e)} \boldsymbol{\varphi}^{(e)} \right].$$
(39)

The element stiffness matrices in the above equation are given by:

$$\mathbf{K}_{\mathbf{u}\mathbf{u}}^{(e)} = AC_{33}^{[s]} \, \widehat{\mathbf{K}}^{(e)}, \qquad \mathbf{K}_{\mathbf{u}\phi}^{(e)} = Ae_{33}^{[s]} \, \widehat{\mathbf{K}}^{(e)}, \qquad \mathbf{K}_{\mathbf{w}\mathbf{w}}^{(e)} = AC_{23}^{[s]} \, \widehat{\mathbf{K}}^{(e)}, \\
\mathbf{K}_{\mathbf{w}\varphi}^{(e)} = -A\kappa C_{23}^{[s]} \, \widetilde{\mathbf{K}}^{(e)}, \qquad \mathbf{K}_{\varphi\mathbf{w}}^{(e)} = \mathbf{K}_{\mathbf{w}\varphi}^{(e)T}, \qquad \mathbf{K}_{\varphi\varphi}^{(e)} = IC_{33}^{[s]} \, \widehat{\mathbf{K}}^{(e)}, \\
\mathbf{K}_{\varphi\phi}^{(e)} = \mathbf{K}_{\mathbf{u}\phi}^{(e)T}, \qquad \mathbf{K}_{\varphi\phi}^{(e)} = -A\chi_{33}^{[s]} \, \widehat{\mathbf{K}}^{(e)}, \qquad (40)$$

where the matrices $\hat{\mathbf{K}}^{(e)}$ and $\tilde{\mathbf{K}}^{(e)}$ are defined by:

$$\widehat{K}_{ij}^{(e)} = \int_{\Omega^{(e)}} \frac{\mathrm{d}N_i^{(e)}}{\mathrm{d}z} \frac{\mathrm{d}N_j^{(e)}}{\mathrm{d}z} \mathrm{d}z, \quad \widetilde{K}_{ij}^{(e)} = \int_{\Omega^{((e))}} \frac{\mathrm{d}N_i}{\mathrm{d}z} N_j \mathrm{d}z. \tag{41}$$

Note that in the notation $\delta W^{[s],(e)}$, the superscripts [s] are used for the beam segment s, and (e) for the integration over the element $\Omega^{(e)}$. It is clear that the element stiffness matrices can be computed via two common matrices $\hat{\mathbf{K}}^{(e)}$ and $\tilde{\mathbf{K}}^{(e)}$.

As for the mass matrices, the variational formulation (31) is used. For one element, it is straightforward to derive:

$$\int_{t_0}^{t_1} \delta T^{[s],(e)} dt = -\int_{t_0}^{t_1} \left[\delta \mathbf{u}^{(e)} \cdot \mathbf{M}_{\mathbf{u}\mathbf{u}}^{(e)} \mathbf{u}_{tt}^{(e)} + \delta \mathbf{w}^{(e)} \cdot \mathbf{M}_{\mathbf{w}\mathbf{w}}^{(e)} \mathbf{w}_{tt}^{(e)} + \delta \boldsymbol{\varphi}^{(e)} \cdot \mathbf{M}_{\boldsymbol{\varphi}\boldsymbol{\varphi}}^{(e)} \boldsymbol{\varphi}_{tt}^{(e)} \right] dt, \tag{42}$$

where:

$$\mathbf{M}_{\mathbf{u}\mathbf{u}}^{(e)} = \mathbf{M}_{\mathbf{w}\mathbf{w}}^{(e)} = A\rho^{[s]} \, \widehat{\mathbf{M}}^{(e)}, \quad \mathbf{M}_{\varphi\varphi}^{(e)} = I\rho^{[s]} \, \widehat{\mathbf{M}}^{(e)}, \quad \widehat{M}_{ij}^{(e)} = \int\limits_{\Omega^{(e)}} N_i^{(e)} N_j^e \, \mathrm{d}z. \tag{43}$$

3.3. Computation of natural frequencies

The global system of discretized governing equations can be obtained by the standard assembly procedure [48]. To this end, the following system for the $\delta \mathbf{u}$, $\delta \mathbf{w}$, and $\delta \boldsymbol{\varphi}$ terms can be generated:

$$\begin{bmatrix} \mathbf{M_{u}} & \mathbf{0} & \mathbf{0} \\ \mathbf{0} & \mathbf{M_{ww}} & \mathbf{0} \\ \mathbf{0} & \mathbf{0} & \mathbf{M_{\varphi\varphi}} \end{bmatrix} \frac{\partial^{2}}{\partial t^{2}} \begin{bmatrix} \mathbf{u} \\ \mathbf{w} \\ \boldsymbol{\varphi} \end{bmatrix} + \begin{bmatrix} \mathbf{K_{uu}} & \mathbf{0} & \mathbf{0} & \mathbf{K_{u\varphi}} \\ \mathbf{0} & \mathbf{K_{ww}} & \mathbf{K_{w\varphi}} & \mathbf{0} \\ \mathbf{0} & \mathbf{K_{\varphi w}} & \mathbf{K_{\varphi\varphi}} & \mathbf{0} \end{bmatrix} \begin{bmatrix} \mathbf{u} \\ \mathbf{w} \\ \boldsymbol{\varphi} \\ \boldsymbol{\phi} \end{bmatrix} = \mathbf{0}$$
(44)

with the equation for $\delta \phi$ as follows:

$$\mathbf{K}_{\phi\mathbf{n}}\mathbf{u} + \mathbf{K}_{\phi\phi}\phi = \mathbf{0} \tag{45}$$

One should recall the remark concerning the reduction of governing equations in Section 2.5.4. Indeed, the argument therein applies also to the discretized system of equations. Accordingly, the degrees of freedom in φ only persists with the beam segment [3], while the degrees of freedom in \mathbf{u} , \mathbf{w} and φ are for the entire transducer beam. This is an important remark in the numerical implementation.

Let us group the degrees of freedom for \mathbf{u} , \mathbf{w} and $\boldsymbol{\varphi}$ into a master column vector \mathbf{d} and group the corresponding stiffness matrices as follows:

$$\mathbf{M_{dd}}\mathbf{d}_{,tt} + \mathbf{K_{dd}}\mathbf{d} + \mathbf{K_{u\phi}}\boldsymbol{\phi} = \mathbf{0},$$

$$\mathbf{K_{\phi u}}\mathbf{u} + \mathbf{K_{\phi \phi}}\boldsymbol{\phi} = \mathbf{0},$$
(46)

with:

$$\mathbf{d} = \begin{bmatrix} \mathbf{u} \\ \mathbf{w} \\ \varphi \end{bmatrix}, \quad \mathbf{M}_{dd} = \begin{bmatrix} \mathbf{M}_{uu} & \mathbf{0} & \mathbf{0} \\ \mathbf{0} & \mathbf{M}_{ww} & \mathbf{0} \\ \mathbf{0} & \mathbf{0} & \mathbf{M}_{\omega\omega} \end{bmatrix}, \quad \mathbf{K}_{dd} = \begin{bmatrix} \mathbf{K}_{uu} & \mathbf{0} & \mathbf{0} \\ \mathbf{0} & \mathbf{K}_{ww} & \mathbf{K}_{w\varphi} \\ \mathbf{0} & \mathbf{K}_{\omega w} & \mathbf{K}_{\omega\omega} \end{bmatrix}$$
(47)

The unknown ϕ can be eliminated from the system by using the second equation (46)₂. Indeed, resolving this equation gives:

$$\phi = -\mathbf{K}_{\phi\phi}^{-1} \mathbf{K}_{\phi\mathbf{u}} \mathbf{u}. \tag{48}$$

Here, the appropriate boundary conditions on the beam segment [3] must be applied to eliminate the singular mode in $\mathbf{K}_{\phi\phi}$. In this consideration, $\phi = V_1$ and $\phi = V_2$ are applied on the left and the right boundaries of the beam segment [3] so that the applied potential voltage is effectively $\Delta\phi := V_2 - V_1$. Substituting (48) into the first equation of (46), the following can be obtained:

$$\mathbf{M}_{dd}\mathbf{d}_{,tt} + \mathbf{K}_{dd}\mathbf{d} + \mathbf{K}_{u\phi}\mathbf{K}_{\phi\phi}^{-1}\mathbf{K}_{\phi u}\mathbf{u} = \mathbf{0}. \tag{49}$$

This equation can be rewritten as:

$$\mathbf{M}_{\mathbf{d}\mathbf{d}}\mathbf{d}_{u} + \hat{\mathbf{K}}_{\mathbf{d}\mathbf{d}}\mathbf{d} = \mathbf{0},\tag{50}$$

with \hat{K}_{dd} being modified from K_{dd} to take into account of the last term $K_{u\phi}K_{\phi\phi}^{-1}K_{\phi u}u$ as follows:

$$\hat{\mathbf{K}}_{dd} = \begin{bmatrix} \mathbf{K}_{uu} - \mathbf{K}_{u\phi} \mathbf{K}_{\phi\phi}^{-1} \mathbf{K}_{\phi u} & \mathbf{0} & \mathbf{0} \\ \mathbf{0} & \mathbf{K}_{ww} & \mathbf{K}_{w\phi} \\ \mathbf{0} & \mathbf{K}_{ww} & \mathbf{K}_{\phi a} \end{bmatrix}$$
(51)

The natural frequencies and the natural displacement modes including both the bending and longitudinal modes are computed by solving the standard eigenvalue problem:

$$[\hat{\mathbf{K}}_{dd} - \omega^2 \mathbf{M}_{dd}] \mathbf{d} = \mathbf{0}. \tag{52}$$

The natural frequencies ω_j and the corresponding natural displacement modes \mathbf{d}_j are the square root of the eigenvalues and the eigenvectors, respectively, of the above eigenvalue problem:

$$\left[\hat{\mathbf{K}}_{dd} - \omega_j^2 \mathbf{M}_{dd}\right] \mathbf{d}_j = \mathbf{0}, \quad j = 1, 2, 3, \dots$$
 (53)

The results ω_j and \mathbf{d}_j will be compared with the eigenfrequencies and eigenmodes computed by using the 3D model and the experimental results in the next section.

4. Results and discussion

4.1. Problem definition

As mentioned in section 2.4.1, the relevant material constants for the 1D constitutive law can be derived using the piezoelectric material constants provided by the manufacturer of the PZT (PIC181, PI Ceramic GmbH). The material properties for the simulations are given in Table 2.

It should be noted that C_{33} and C_{23} shown in (2) for the PIC181 material are not the Young's modulus and shear modulus, but instead are computed by (4). On the other hand, as for the isotropic elastic material, E can be assigned to C_{33} and $G = \frac{E}{2(1+\nu)}$ to C_{23} as above.

Table 2
Material properties of A2 Tool Steel, Ti6Al4V, and PIC181, where Voigt notation has been used where relevant.

| Material properties | A2 Tool Steel | Ti6Al4V | PIC181 | |
|------------------------------|---------------|---------|-----------------------|--|
| ρ (kg/m ³) | 7860 | 4430 | 7800 | |
| E (GPa) | 203 | 109 | - | |
| ν | 0.285 | 0.313 | 0.34 | |
| C_{33} (GPa) | - | - | 121.7 | |
| C_{23} (GPa) | - | - | 26.3 | |
| e_{33} (C/m ²) | - | - | 18.7 | |
| X ₃₃ | - | - | 1.06×10^{-8} | |

Table 3
Structural dimensions.

| Parameters | Dimension |
|---------------------|--------------------|
| l ₁ (mm) | 0.5D |
| l_2 (mm) | $0.5(L-l_1-l_3)$ |
| l_3 (mm) | $0.05L \sim 0.25L$ |
| l_4 (mm) | l_2 |
| l_5 (mm) | $0.5l_4$ |
| d (mm) | 0.5D |
| D_B (mm) | 0.75D |

The dimensions of different beam segments are given in the Table 3. The total length of the transducer is $L = \sum_{i=1}^{3} l_i = 100$ mm. The electrical potentials $\phi = V_1$ and $\phi = V_2$ with $(V_2 > V_1)$ were applied on the two ends of the PZT stack, so the potential difference is $\Delta \phi = V_2 - V_1$. To demonstrate the robustness of the proposed computational framework as compared to the full 3D model, multiple simulations are performed corresponding to different geometrical settings by varying two ratios D/L and l_3/L and also the electric potential difference $\Delta \phi$.

4.2. Comparison with three-dimensional model

The comparisons between the solutions of the 1D and 3D models are established by varying the following:

- L/D in the set $\mathcal{D}_{L/D} = \{5, 10, 25/2, 20, 25\},\$
- l_3/L in the set $\mathcal{D}_{l_3/L} = \{1/20, 1/10, 3/20, 1/5, 1/4\},$
- $\Delta \phi$ in the set $\mathcal{D}_{\Delta \phi} = \{0, 50, 100\}V$.

Thus, $5 \cdot 5 \cdot 3 = 75$ simulations are performed for both 1D and 3D model problems, where the first five bending modes and the first five longitudinal mode resonance frequencies for each problem setting are collected. Also, the two ends of the transducer are set to be free. Assuming that the front mass and the back mass block have equal lengths, and the dimensions of the bolt follow the standard ISO 4762:2004 for a hexagon socket head cap screw, the structural parameters of the transducer can be deduced. The formulas in Table 3 express the correlation between all the structural parameters, namely d, D_B , D and l_j . The relative difference between the resonance frequency obtained by the 1D model and the corresponding value by the 3D model is then computed.

The natural frequencies of the first five bending modes and the first five longitudinal modes obtained by the proposed 1D model are compared with the corresponding counterparts obtained by the full 3D model. The relative difference between the frequency of the 1D and 3D models, denoted as $f_{\rm 1D}$ and $f_{\rm 3D}$, is computed according to $(f_{\rm 1D}-f_{\rm 3D})/f_{\rm 3D}$. The relative differences shown in Fig. 5 are generally below 5%, except for the relatively high longitudinal mode frequencies in the case of L/D=5. The relative difference increases as the vibration modes increase, regardless of whether they are bending modes or longitudinal modes. Overall, the relative differences decrease with increasing ratio L/D and change insignificantly with the change of the ratio I_3/L . The relative differences are particularly high for the small ratio L/D=5 but rather acceptably small for the ratio L/D=10. Indeed, when L/D is small, the full 3D model should give a distinctive result from the 1D model.

However, both the L/D ratio and the l_3/L ratio of the transducer influence the accuracy of the results of the 1D model. It has been observed that the relative difference of the modes tends to significantly decrease with an increase in the L/D ratio, especially increasing the L/D ratio from 5 to 10. When the transducer is rather slender with $L/D \ge 12.5$, the computed natural frequencies of the 1D model agree with the results of the 3D model very well, which justifies the reliability of the proposed computational framework. Moreover, the l_3/L ratio has a smaller impact on the resonance frequency compared to that of the L/D ratio. Still, it has an obvious influence on resonance frequencies when the L/D ratio is 5. Furthermore, it is arguable that the applied electric voltage $\Delta \phi$ has little impact on the relative difference. In fact, it only affects resonance frequencies on a small scale, around 10^{-2} . Nevertheless, if the applied electric voltage is very high, in effect beyond the normal application range, it can still significantly influence the natural frequency corresponding to the longitudinal mode.

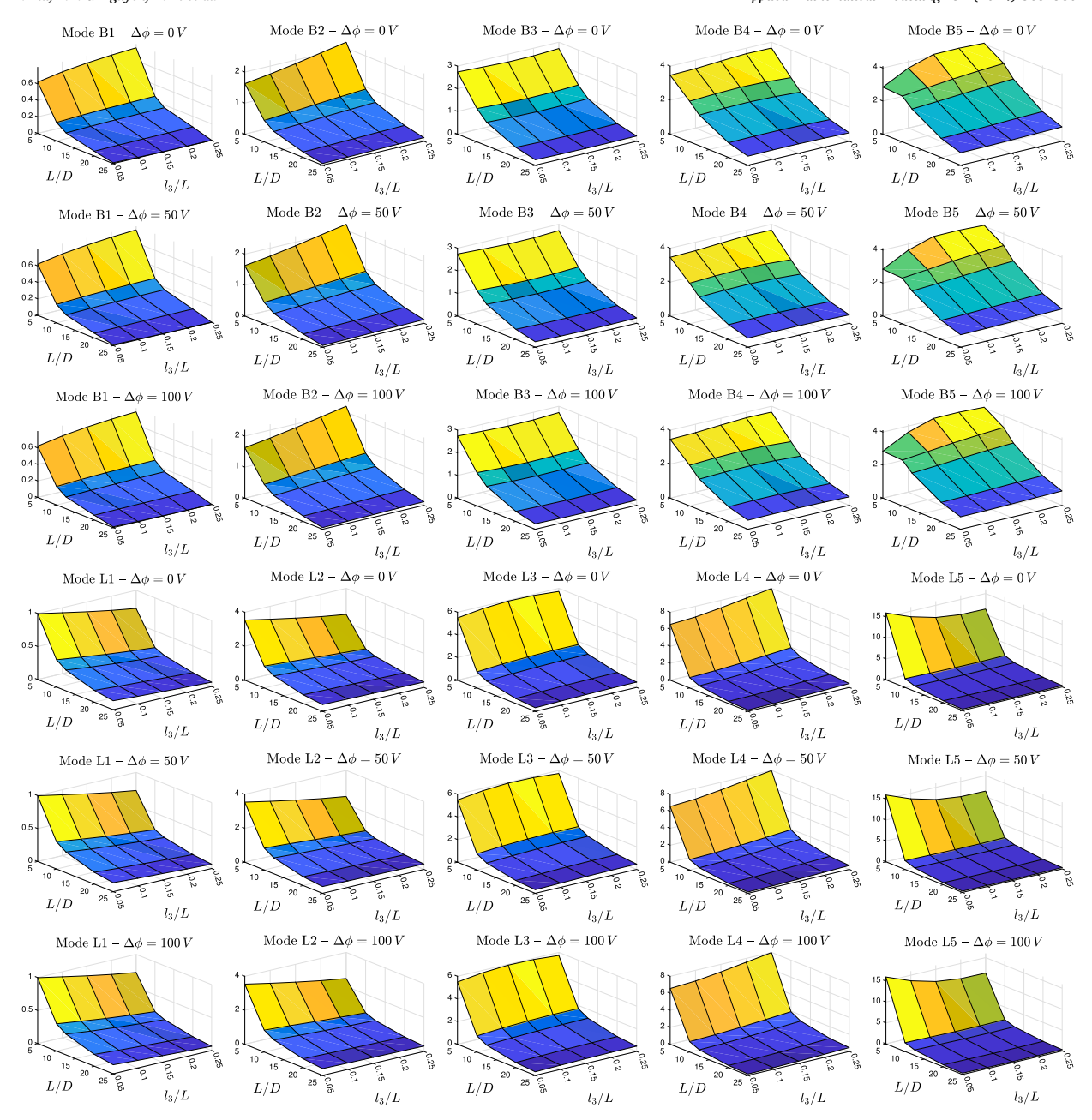


Fig. 5. Relative differences between the results of 1D and 3D models for the first ten vibration modes with respect to the L/D ratio, l_3/L ratio, and electric potential $\Delta\phi$. In this figure, the letter B in the title stands for 'bending mode' and L for the 'longitudinal mode'. For example, B1 and L1 mean the 1st bending and longitudinal modes, respectively.

4.3. Comparison with experiment

To verify the 1D model for solving Langevin transducer dynamics, a Langevin transducer was designed and manufactured with an L/D ratio in the order of 12.5 and a l_3/L ratio of approximately 0.05. The transducer is shown in Fig. 6. It consists of a titanium front mass, titanium back mass, PZT stack composed of PIC181, and preloading bolt made of A2 tool steel. All material properties are identical to those listed in Table 2.

The dimensions of the Langevin transducer prototype are listed in Table 4. In order to measure resonance frequencies, mode shapes, and vibration amplitudes, an optical measurement experiment was conducted using the 3D LDV (MSA100, Polytec) under an 8V excitation. For this study, experimental measurements for the first ten longitudinal and bending modes were considered and extracted. Calculations were performed to obtain the resonance frequencies for the 1D and 3D models based on the physical structural parameters in Table 4. The comparison between the simulation results and the experimental measurements is shown Table 5. The

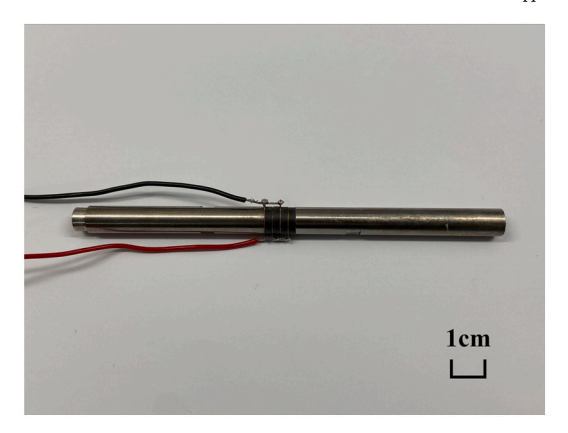


Fig. 6. The Langevin transducer prototype.

 Table 4

 Dimensions of the Langevin transducer prototype.

| Parameters | Dimension | | |
|---------------------|-----------|--|--|
| l ₁ (mm) | 4 | | |
| l_2 (mm) | 51.5 | | |
| l_3 (mm) | 9.2 | | |
| l_4 (mm) | 40.5 | | |
| l_5 (mm) | 19 | | |
| | | | |

| Parameters | Dimension |
|------------|-----------|
| D (mm) | 8 |
| d (mm) | 4 |
| D_B (mm) | 7 |

Table 5
Comparison of resonance frequencies obtained by 1D model, 3D model and LDV measurements. In this table, the letter B in the column mode stands for 'bending mode' and L for the 'longitudinal mode'. For example, B1 and L1 mean the 1st bending and longitudinal modes, respectively. The second row shows how the relative differences in percentages are computed. The frequencies are listed in ascending order of magnitude.

| Mode | 1D Model (Hz) | 3D Model (Hz) | LDV (Hz) | 1D Model vs. 3D Model (%) | 1D Model vs. LDV (%) | 3D Model vs. LDV (%) |
|------|------------------|------------------|-------------|------------------------------------|-------------------------------|-------------------------------|
| B1 | 2111.4807 | 2113.9980 | 2031 | 0.1191 | 3.9626 | 4.0866 |
| B2 | 5926.9478 | 5933.2798 | 6230 | 0.1067 | 4.8644 | 4.7628 |
| В3 | 10566.6597 | 10638.2324 | 10459 | 0.6728 | 1.0294 | 1.7137 |
| B4 | 17649.8388 | 17748.2871 | 18770 | 0.5547 | 5.9678 | 5.4433 |
| L1 | 20702.1092 | 20670.4668 | 19277 | 0.1531 | 7.3928 | 7.2286 |
| B5 | 24481.3235 | 24880.9141 | 26045 | 1.6060 | 6.0037 | 4.4695 |
| В6 | 33864.6709 | 34310.3633 | 34395 | 1.2990 | 1.5419 | 0.2461 |
| L2 | 40195.6881 | 40012.6758 | 38213 | 0.4574 | 5.1885 | 4.7096 |
| В7 | 42198.0625 | 43228.8828 | 44063 | 2.3846 | 4.2324 | 1.8930 |
| B8 | 52180.8544 | 53183.7109 | 52285 | 1.8856 | 0.1992 | 1.7189 |

symbols 'L' and 'B' in the table represent the longitudinal and bending modes, respectively, and the number following the letter indicates the eigenmode order, where the reader is directed to the caption for examples.

According to Table 5, it has been found that 1D and 3D models give results in excellent agreement, and both match with LDV results, indicating the accuracy and reliability of the 1D model in calculating resonance frequencies of a Langevin transducer. Except for the L1 mode, both 1D and 3D models have a relative difference from LDV results that is less than 5%. The results from the 3D model are closer with LDV results than the 1D model in most of the considered modes. The relative differences with LDV results are principally due to manufacturing inconsistencies and the inclusion of electrodes in the PZT stack. Additionally, the modelling theory presented here cannot capture all of the physical phenomena. For example, we did not consider the losses in piezoelectric materials, while this effect may occur in the experiment.

For further validation, the 1D model was compared to the 3D model and LDV results in terms of vibration mode shapes for the first ten modes. The results expressed in normalized amplitudes are shown in Fig. 7.

The normalized amplitude calculated by the 1D model matches that of the 3D model, with a very good agreement with the LDV results. This confirms that the 1D model can accurately describe the dynamics of a Langevin transducer, either in terms of resonance frequency or the vibration mode shapes. Overall, the performance of the proposed 1D model is particularly suitable for engineering applications that typically utilise low-order vibration modes.

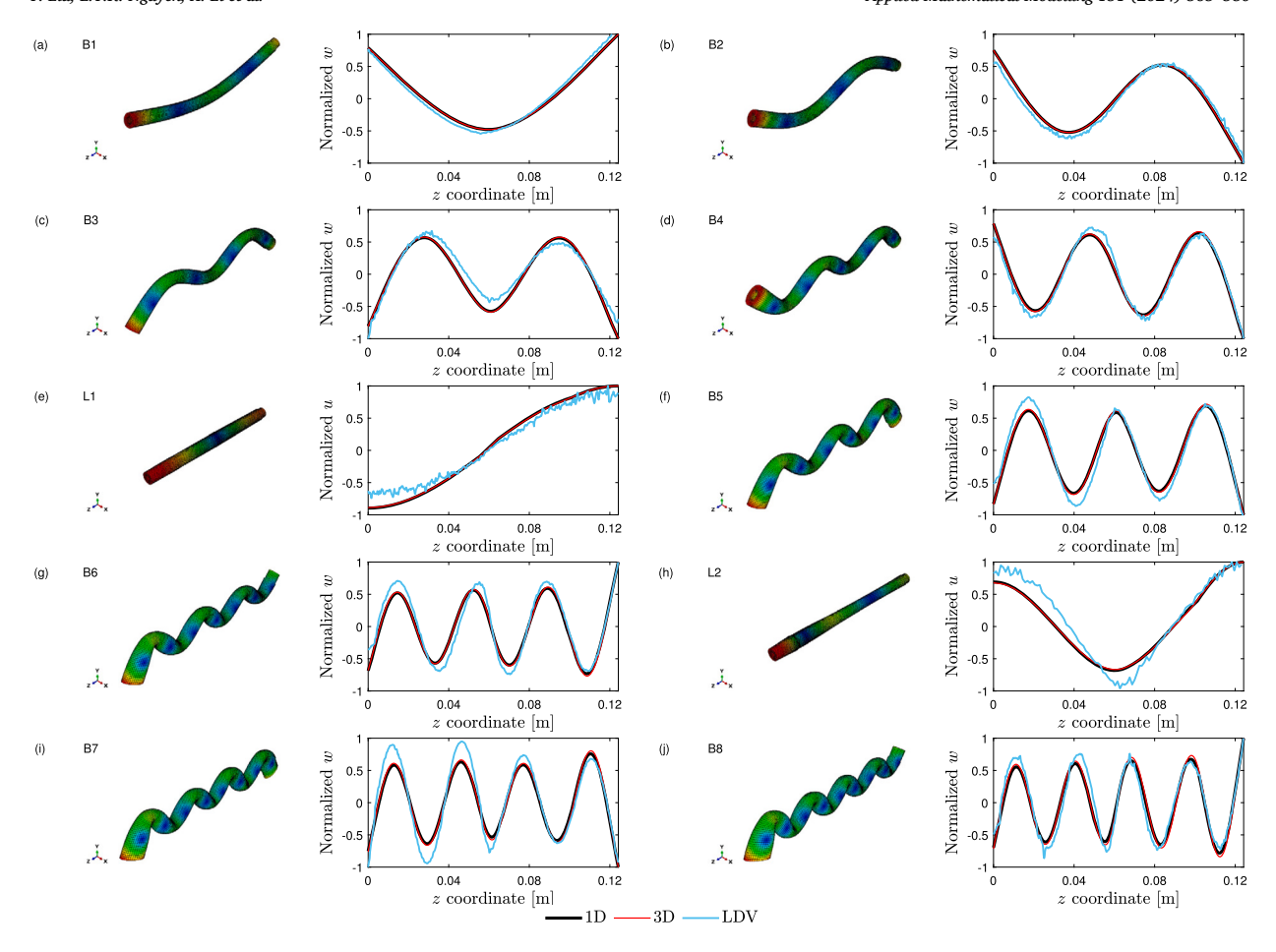


Fig. 7. Normalized vibration amplitudes and mode shapes between 1D model (numerical), 3D model (FEA), and LDV results.

The advantage of the 1D variational framework proposed in this study is that it simplifies the problem by reducing it to one dimension, as the transducer is axisymmetric. This allows for a more efficient and straightforward analysis of the linear piezoelectricity compared to higher-dimensional frameworks [51,52]. However, the Timoshenko-Ehrenfest beam theory assumes that the cross-section remains in-plane when subjected to shear forces, and is a downside of the 1D variational framework for considering average shear deformation. Nevertheless, the eigenfrequency difference compared to the 3D model can be neglected if the L/D ratio is sufficiently large. Additionally, the 1D variational framework makes it easier to visualize the normalized deformation, making it a more accessible approach to understanding the electromechanical properties of Langevin transducers.

5. Conclusion

In this study, the dynamics of a Langevin transducer were derived mathematically, through a new electromechanical model which fully accounts for the axial strains across the entire transducer. The configuration of the transducer was divided into five segments, each with a solid or composite beam structure. To construct the model, a reduced 1D Timoshenko-Ehrenfest beam model was employed. Then, a variational framework was developed based on the constitutive law in strain-charge form, which describes the piezoelectric material. By using Hamilton's principle, the governing equations were then derived, after which the corresponding variational framework was discretized and solved using the spectral element method. The results show that the 1D model is robust for predicting the dynamic behaviour of various structural configurations, with a relative difference lower than 5% between the 1D and 3D models. Importantly, the close correlation of the resonance frequencies and mode shapes between the 1D, 3D, and LDV results validates the applicability of the new 1D model in the design, manufacture, and characterisation of the Langevin transducer.

Declaration of competing interest

The authors declare that they have no known competing financial interests or personal relationships that could have appeared to influence the work reported in this paper.

Data availability

Data will be made available on request.

Acknowledgements

This work was supported by the Engineering and Physical Sciences Research Council (Grant EP/V049658/1).

References

- [1] A. Cardoni, A. MacBeath, M. Lucas, Methods for reducing cutting temperature in ultrasonic cutting of bone, Ultrasonics 44 (2006) e37–e42, https://doi.org/10.1016/j.ultras.2006.06.046.
- [2] F. Bejarano, A. Feeney, R. Wallace, H. Simpson, M. Lucas, An ultrasonic orthopaedic surgical device based on a cymbal transducer, Ultrasonics 72 (2016) 24–33, https://doi.org/10.1016/j.ultras.2016.07.004.
- [3] R. Cleary, R. Wallace, H. Simpson, G. Kontorinis, M. Lucas, A longitudinal-torsional mode ultrasonic needle for deep penetration into bone, Ultrasonics 124 (2022) 106756, https://doi.org/10.1016/j.ultras.2022.106756.
- [4] S. Dong, W. Liao, K. Zheng, J. Liu, J. Feng, Investigation on exit burr in robotic rotary ultrasonic drilling of cfrp/aluminum stacks, Int. J. Mech. Sci. 151 (2019) 868–876, https://doi.org/10.1016/j.ijmecsci.2018.12.039.
- [5] J. Dassow, X. Li, M. Lee, M. Young, P. Harkness, Ultrasonic drilling for the characterisation of building stones and salt induced decay, Ultrasonics 101 (2020) 106018, https://doi.org/10.1016/j.ultras.2019.106018.
- [6] N. Mikhailova, P. Onawumi, G. Volkov, I. Smirnov, M. Broseghini, A. Roy, Y. Petrov, V. Silberschmidt, Ultrasonically assisted drilling in marble, J. Sound Vib. 460 (2019) 114880, https://doi.org/10.1016/j.jsv.2019.114880.
- [7] N.A. Muhammad, C. Wu, Evaluation of capabilities of ultrasonic vibration on the surface, electrical and mechanical behaviours of aluminium to copper dissimilar friction stir welds, Int. J. Mech. Sci. 183 (2020) 105784, https://doi.org/10.1016/j.ijmecsci.2020.105784.
- [8] H.-T. Nguyen, H.-D. Nguyen, J.-Y. Uan, D.-A. Wang, A nonrational b-spline profiled horn with high displacement amplification for ultrasonic welding, Ultrasonics 54 (8) (2014) 2063–2071, https://doi.org/10.1016/j.ultras.2014.07.003.
- [9] S.K. Bhudolia, G. Gohel, K.F. Leong, A. Islam, Advances in ultrasonic welding of thermoplastic composites: a review, Materials 13 (6) (2020) 1284, https://doi.org/10.3390/ma13061284.
- [10] X. Li, T. Stritch, K. Manley, M. Lucas, Limits and opportunities for miniaturizing ultrasonic surgical devices based on a Langevin transducer, IEEE Trans. Ultrason. Ferroelectr. Freq. Control 68 (7) (2021) 2543–2553, https://doi.org/10.1109/TUFFC.2021.3065207.
- [11] J. Kim, J. Lee, Parametric study of bolt clamping effect on resonance characteristics of Langevin transducers with lumped circuit models, Sensors 20 (7) (2020) 1952, https://doi.org/10.3390/s20071952.
- 1952, https://doi.org/10.3590/8200/1952.
 [12] T. Harada, N. Ishikawa, T. Kanda, K. Suzumori, Y. Yamada, K.-I. Sotowa, Droplet generation using a torsional Langevin-type transducer and a micropore plate,
- Sens. Actuators A, Phys. 155 (1) (2009) 168–174, https://doi.org/10.1016/j.sna.2009.08.007.
 [13] C.-H. Yun, T. Ishii, K. Nakamura, S. Ueha, K. Akashi, A high power ultrasonic linear motor using a longitudinal and bending hybrid bolt-clamped Langevin type transducer, Jpn. J. Appl. Phys. 40 (5S) (2001) 3773, https://doi.org/10.1143/JJAP.40.3773.
- [14] V. Ostasevicius, V. Jurenas, S. Mikuckyte, J. Vezys, E. Stankevicius, A. Bubulis, M. Venslauskas, L. Kizauskiene, Development of a low-frequency piezoelectric ultrasonic transducer for biological tissue sonication, Sensors 23 (7) (2023) 3608, https://doi.org/10.3390/s23073608.
- [15] A. Mathieson, A. Cardoni, N. Cerisola, M. Lucas, The influence of piezoceramic stack location on nonlinear behavior of Langevin transducers, IEEE Trans. Ultrason. Ferroelectr. Freq. Control 60 (6) (2013) 1126–1133, https://doi.org/10.1109/TUFFC.2013.2675.
- [16] K. Zhang, G. Gao, C. Zhao, Y. Wang, Y. Wang, J. Li, Review of the design of power ultrasonic generator for piezoelectric transducer, Ultrason. Sonochem. (2023)
- 106438, https://doi.org/10.1016/j.ultsonch.2023.106438.
 [17] P. Harkness, M. Lucas, A. Cardoni, Coupling and degenerating modes in longitudinal-torsional step horns, Ultrasonics 52 (8) (2012) 980–988, https://doi.org/
- 10.1016/j.ultras.2012.05.002. [18] E. Heikkola, M. Laitinen, Model-based optimization of ultrasonic transducers, Ultrason. Sonochem. 12 (1–2) (2005) 53–57, https://doi.org/10.1016/j.ultsonch.
- 2004.05.009.
 [19] A. Pérez-Sánchez, J. Segura, C. Rubio-Gonzalez, L.A. Baldenegro-Pérez, J. Soto-Cajiga, Numerical design and analysis of a Langevin power ultrasonic transducer for acoustic cavitation generation, Sens. Actuators A, Phys. 311 (2020) 112035, https://doi.org/10.1016/j.sna.2020.112035.
- [20] J.O. Kim, O.S. Kwon, Vibration characteristics of piezoelectric torsional transducers, J. Sound Vib. 264 (2) (2003) 453–473, https://doi.org/10.1016/S0022-460X(02)01234-8.
- [21] Y. Liu, M. Hafezi, A. Feeney, A cascaded nitinol Langevin transducer for resonance stability at elevated temperatures, Ultrasonics 137 (2024) 107201, https://doi.org/10.1016/j.ultras.2023.107201.
- [22] S. Zhang, Y. Li, S. Li, Y. Wu, J. Zeng, Investigation of the nonlinear phenomena of a Langevin ultrasonic transducer caused by high applied voltage, Proc. Inst. Mech. Eng., Part C, J. Mech. Eng. Sci. 236 (2) (2022) 873–885, https://doi.org/10.1177/09544062211009343.
- [23] H. Qi, D. Fang, Z. Yao, Fem analysis of electro-mechanical coupling effect of piezoelectric materials, Comput. Mater. Sci. 8 (4) (1997) 283–290, https://doi.org/10.1016/S0927-0256(97)00041-4.
- [24] J. Schröder, D. Gross, Invariant formulation of the electromechanical enthalpy function of transversely isotropic piezoelectric materials, Arch. Appl. Mech. 73 (2004) 533–552, https://doi.org/10.1007/s00419-003-0294-5.
- [25] D. Damjanovic, R. Newnham, Electrostrictive and piezoelectric materials for actuator applications, J. Intell. Mater. Syst. Struct. 3 (2) (1992) 190–208, https://doi.org/10.1177/1045389X9200300201.
- [26] P. Yu, L. Wang, S. Zhang, J. Jin, Transfer matrix modeling and experimental verification of forked piezoelectric actuators, Int. J. Mech. Sci. 232 (2022) 107604, https://doi.org/10.1016/j.ijmecsci.2022.107604.
- [27] L. Wang, J.-A. Wang, J.-M. Jin, L. Yang, S.-W. Wu, C.C. Zhou, Theoretical modeling, verification, and application study on a novel bending-bending coupled piezoelectric ultrasonic transducer, Mech. Syst. Signal Process. 168 (2022) 108644, https://doi.org/10.1016/j.ymssp.2021.108644.
- [28] G. Chen, X. Zeng, X. Liu, X. Rui, Transfer matrix method for the free and forced vibration analyses of multi-step Timoshenko beams coupled with rigid bodies on springs, Appl. Math. Model. 87 (2020) 152–170, https://doi.org/10.1016/j.apm.2020.05.023.
- [29] A. Cornogolub, P.-J. Cottinet, L. Petit, Analytical modeling of curved piezoelectric, Langevin-type, vibrating transducers using transfer matrices, Sens. Actuators A, Phys. 214 (2014) 120–133, https://doi.org/10.1016/j.sna.2014.04.003.
- [30] X. Li, Z. Yao, Analytical modeling and experimental validation of a v-shape piezoelectric ultrasonic transducer, Smart Mater. Struct. 25 (7) (2016) 075026, https://doi.org/10.1088/0964-1726/25/7/075026.
- [31] M. Karafi, S. Kamali, A continuum electro-mechanical model of ultrasonic Langevin transducers to study its frequency response, Appl. Math. Model. 92 (2021) 44–62, https://doi.org/10.1016/j.apm.2020.11.006.

- [32] H. Al-Budairi, M. Lucas, P. Harkness, A design approach for longitudinal-torsional ultrasonic transducers, Sens. Actuators A, Phys. 198 (2013) 99–106, https://doi.org/10.1016/j.sna.2013.04.024.
- [33] S. Darbasi, A.M. Abazari, G. Rezazadeh, Mechanical analysis of a tunable capacitive ultrasound transducer using higher order gradient theory, Appl. Math. Model. 102 (2022) 564–577, https://doi.org/10.1016/j.apm.2021.09.031.
- [34] Y.K.Y. Koike, T.T.T. Tamura, S.U.S. Ueha, Electrical equivalent circuit of loaded thick Langevin flexural transducer, Jpn. J. Appl. Phys. 36 (58) (1997) 3121, https://doi.org/10.1143/JJAP.36.3121.
- [35] K. Uchino, Advanced Piezoelectric Materials: Science and Technology, Woodhead Publishing, 2017.
- [36] Q. Qin, Advanced Mechanics of Piezoelectricity, Springer Science & Business Media, 2012.
- [37] S.W.R. Hamilton, On a General Method in Dynamics, Richard Taylor United Kindom, 1834.
- [38] H. Tzou, J. Zhong, A linear theory of piezoelastic shell vibrations, J. Sound Vib. 175 (1) (1994) 77-88, https://doi.org/10.1006/jsvi.1994.1312.
- [39] K. Yuan, W. Zhu, Full-Field Operating Deflection Shape Measurement of a Structure with a Curved Surface Using a Three-Dimensional Continuously Scanning Laser Doppler Vibrometer System, ASME International Mechanical Engineering Congress and Exposition, vol. 86625, American Society of Mechanical Engineers, 2022, p. V001T01A038, https://doi.org/10.1115/IMECE2022-94706.
- [40] I. Elishakoff, Handbook on Timoshenko-Ehrenfest Beam and Uflyand-Mindlin Plate Theories, World Scientific, 2020.
- [41] Y. Tang, H. Qing, Elastic buckling and free vibration analysis of functionally graded Timoshenko beam with nonlocal strain gradient integral model, Appl. Math. Model. 96 (2021) 657–677, https://doi.org/10.1016/j.apm.2021.03.040.
- [42] Ieee standard on piezoelectricity, ANSI/IEEE Std 176-1987, https://doi.org/10.1109/IEEESTD.1988.79638. 1988.
- [43] C. Wang, S. Kitipornchai, C. Lim, M. Eisenberger, Beam bending solutions based on nonlocal Timoshenko beam theory, J. Eng. Mech. 134 (6) (2008) 475–481, https://doi.org/10.1061/(ASCE)0733-9399(2008)134:6(475).
- [44] N. Van Rensburg, A. Van der Merwe, Natural frequencies and modes of a Timoshenko beam, Wave Motion 44 (1) (2006) 58–69, https://doi.org/10.1016/j.wavemoti.2006.06.008.
- [45] S.S. Rao, Vibration of Continuous Systems, John Wiley & Sons, 2019.
- [46] J. Hutchinson, Shear coefficients for Timoshenko beam theory, J. Appl. Mech. 68 (1) (2001) 87-92, https://doi.org/10.1115/1.1349417.
- [47] J. Banerjee, A. Ananthapuvirajah, Coupled axial-bending dynamic stiffness matrix for beam elements, Comput. Struct. 215 (2019) 1–9, https://doi.org/10.1016/j.compstruc.2019.01.007.
- [48] K.-J. Bathe, Finite Element Procedures, Klaus-Jurgen Bathe, 2006.
- [49] C. Pozrikidis, Introduction to Finite and Spectral Element Methods Using MATLAB, CRC Press, 2005.
- [50] L.N. Trefethen, Spectral Methods in MATLAB, SIAM, 2000.
- [51] H. Allik, T.J. Hughes, Finite element method for piezoelectric vibration, Int. J. Numer. Methods Eng. 2 (2) (1970) 151-157.
- [52] S.-T. Gu, L. Qin, Variational principles and size-dependent bounds for piezoelectric inhomogeneous materials with piezoelectric coherent imperfect interfaces, Int. J. Eng. Sci. 78 (2014) 89–102.